Supplementary Material

Appendix A

This Appendix gives examples of RTK command lines for each utilized RTK algorithm.

Creating the geometry file from the xml files generated during the acquisition:
~\rtkelektasynergygeometry -xml ~_Frames.xml -o ~\geometry.xml

Merging the projections into one file. The cropping options were only used for the H&N image quality phantom (see Chapter 2.6). The parameter I0 (initial intensity) was set to the median of the gain files adjusted to exposure settings (mAs)
~\rtkprojections -p ~\ -r .*.his -o ~\projections.nii -nsort *-lowercrop 0,48 -uppercrop 0,100* -i0 7413

FDK
~\rtkfdk -g ~\ geometry.xml -p ~\ -r projections.nii -o ~\ImageFDK.nii -pad=0.1 -hann=1.0
-dimension 400,256,400

4DRooster SE (total variation)
~\rtkfourdrooster -p ~\ -r projections.nii -g ~\ geometry.xml -o ~\ Image4DroosterSE.nii
-signal ~\signal.txt -frames 2 -fp CudaRayCast -bp CudaVoxelBased -n 10 -cgiter 10 -gamma_space 1e-4
-dimension 400,256,400

4DRooster DE (total nuclear variation)
Before reconstruction the geometry and projection files for the low and high energy acquisitions are merged.
~\rtkfourdrooster -p ~\ -r projections_merged.nii -g ~\ geometry_merged.xml
-o ~\ Image4DroosterDE.nii -signal ~\signal.txt -frames 2 -fp CudaRayCast -bp CudaVoxelBased -n 10
-cgiter 10 -gamma_tnv 1e-4 -dimension 400,256,400

Appendix B

This Appendix presents the results of the CTDI measurements for the different CTDI phantom set-ups. The generated mAs-$CTDI_w$ functions were used to derive the mA-ms combinations for the image quality phantom (IQP) and human male phantom (HMP). The resultant $CTDI_w$ and low-high energy dose allocations for the IQP and HMP are also shown.

Table B.1 Acquisition parameters for the repeatability and linearity tests for the CTDI measurements. Both test were performed with the pelvis configuration of the CTDI phantom and with 120kV.

Test	mA	ms	Total mAs	D center [mGy]	D center [mGy/100mAs]
Repeatability	20	20	266	33.77	1.270
	20	20	261.2	33.37	1.278
	20	20	263.6	33.64	1.276
Linearity	0	0		0	
	20	20		263.6	
	20	40		546.4	
	40	40		1131.2	

Table B.2 Acquisition parameters for the CTDI measurements. The number of projections for the various acquisitions varied slightly. To determine the $CTDI_w$ the doses were scaled to the nominal number of projections.

Phantom	kV	mA	ms	Nominal N_{proj}	D center [mGy]	D left [mGy]	D right [mGy]	D bottom [mGy]	D top [mGy]
H&N	120	20	40	330	10.4	11.6	10.8	11.0	11.3
	70	20	40	330	1.6	2.0	1.8	1.8	1.9
	130	20	40	330	12.8	14.2	13.1	13.3	13.8
Pelvis	120	40	40	660	13.8	27.6	22.7	21.8	24.5
	70	40	40	660	1.7	4.4	3.8	3.5	3.8
	130	40	40	660	17.3	31.7	28.0	26.8	28.4
Pelvis + Cu	130	40	40	660	3.4	5.2	4.7	4.7	4.8

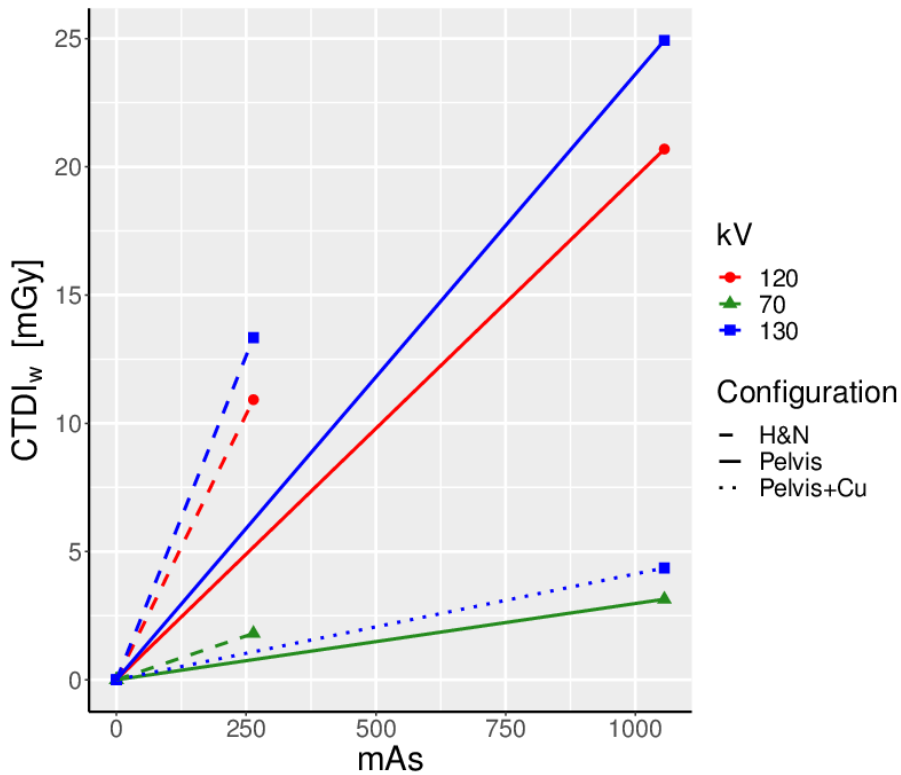

Figure B.1 $CTDI_w$ as a function of mAs for the three energies and two CTDI phantom configurations with and without copper filtration.

Table B.3 Acquisition parameters, the resulting $CTDI_w$ and dose percentages for the H&N image quality phantom (IQP) configuration. While the combinations were determined with the nominal number of projections, the results are shown for the measured number of projections N_{proj}.

Phantom	**kV**	**mA**	**ms**	**N_{proj}**	**$CTDI_w$ [mGy]**	**Dose [%]**
IQP H&N	120	16	40	342	9.0	100
	70	100	40	343	9.4	100
	130	16	32	344	8.9	100
	70	20	40	343	1.9	21
	130	20	20	341	6.9	79
	70	40	40	171	1.9	21
	130	32	25	170	6.9	79
	70	40	32	345	3.0	35
	130	16	20	340	5.5	65
	70	80	32	173	3.0	35
	130	32	20	170	5.5	65
	70	100	40	172	4.7	51
	130	16	32	172	4.5	49
	70	64	32	343	4.8	52

130	16	16	340	4.4	48
70	160	40	173	7.6	77
130	16	16	170	2.2	23
70	80	40	344	7.5	81
130	10	10	342	1.7	19

Table B.4 Acquisition parameters, the resulting $CTDI_w$ and dose percentages for the pelvis image quality phantom (IQP) configuration with and without added copper beam filtration.

Phantom	**kV**	**mA**	**ms**	**N_{proj}**	**$CTDI_w$ [mGy]**	**Dose [%]**
IQP pelvis	120	32	40	698	17.5	100
	70	200	40	702	16.7	100
	130	80	12	698	15.8	100
	70	40	40	698	3.3	20
	130	25	32	700	13.2	80
	70	80	40	353	3.4	20
	130	40	40	348	13.1	80
	70	80	40	705	6.7	39
	130	25	25	700	10.3	61
	70	160	40	353	6.7	39
	130	32	40	348	10.5	61
	70	125	40	679	10.1	57
	130	12	40	675	7.6	43
	70	160	40	706	13.4	72
	130	16	20	693	5.2	28
	70	200	40	702	16.4	88
	130	12	12	699	2.4	12
IQP pelvis with Cu filtration	70	40	40	702	3.3	20
	130	125	40	670	13.8	80
	70	64	40	648	4.9	31
	130	100	40	663	10.9	69
	70	100	40	680	8.1	49
	130	80	40	645	8.5	51
	70	125	40	658	9.8	64
	130	64	32	646	5.4	36
	70	160	40	662	12.6	79
	130	40	32	645	3.4	21

Table B.5 Acquisition parameters, the resulting $CTDI_w$ and dose percentages for the Virtually Human Male Pelvis Phantom (HMP).

Phantom	kV	mA	ms	N_{proj}	$CTDI_w$ [mGy]	Dose [%]
HMP	120	32	40	681	17.1	100
	70	200	40	636	15.1	100
	130	80	12	671	15.2	100
	70	80	40	337	3.2	19
	130	40	40	360	13.6	81
	70	40	40	650	3.1	20
	130	25	32	669	12.6	80
	70	160	40	343	6.5	39
	130	32	40	337	10.2	61
	70	80	40	673	6.4	39
	130	25	25	672	9.9	61
	70	125	40	674	10.0	55
	130	12	40	727	8.2	45
	70	160	40	686	13.0	72
	130	16	20	680	5.1	28
	70	200	40	641	15.2	87
	130	12	12	679	2.3	13

Appendix C

This Appendix visualizes the determination of the CNR and spatial frequency for the two utilized phantoms.

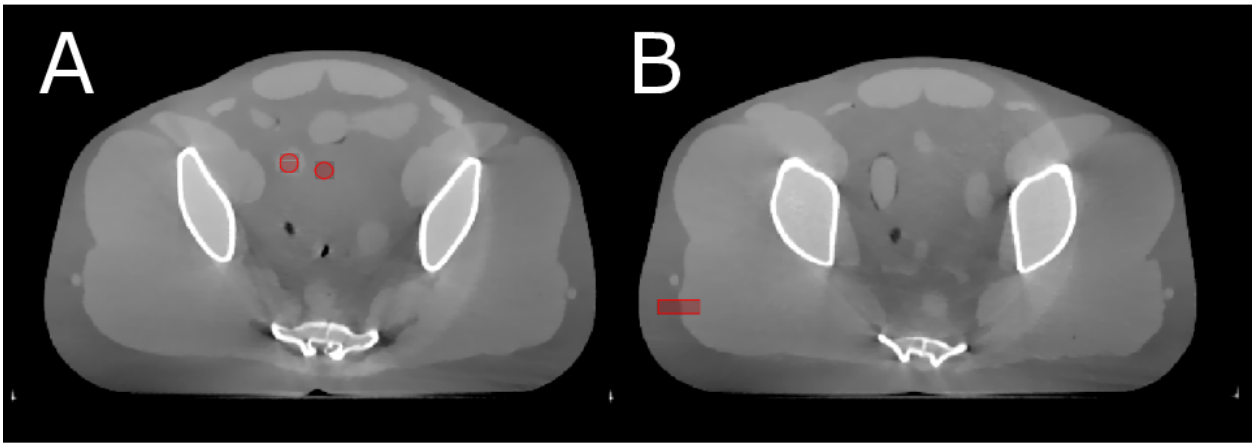

Figure C.1 Positions of the volumes of interest for the contrast-to-noise ratio determination (A) and the area that was used to determine the edge response (B) for the Virtually Human Male Pelvis Phantom.

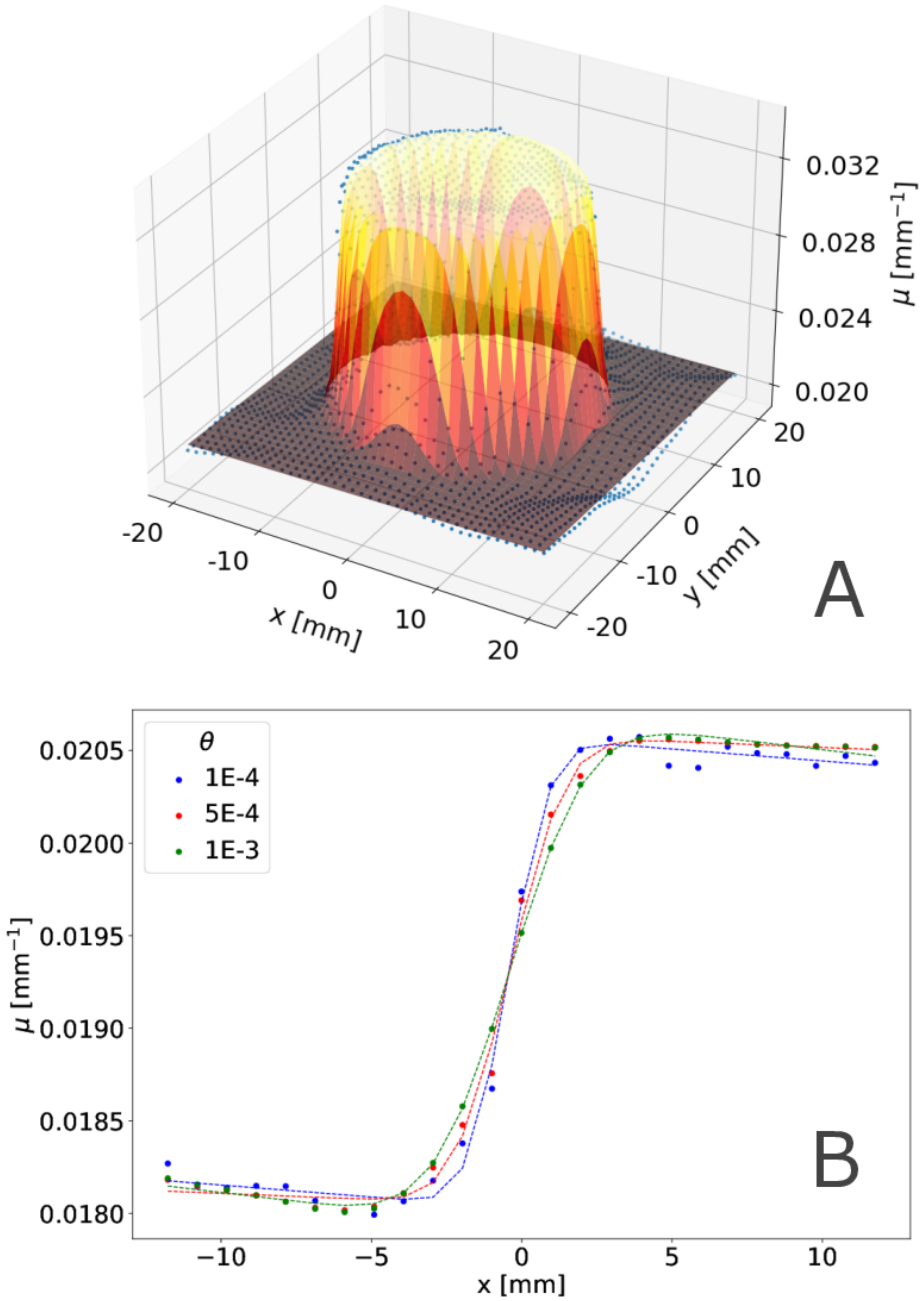

Figure C.2 (A) 2D fit (Eq. 9) of the region of interest including the Teflon insert used to determine the spatial frequency for the Image Quality Phantom, exemplarily shown for the pelvis configuration, $DA_{57\%/43\%}$, LE component, N=10, $\theta=10^{-3}$. (B) 1D fit of the edge response to determine the spatial frequency for the Virtually Human Male Pelvis Phantom, exemplarily shown for $DA_{55\%/45\%}$, LE component, N=10.

Appendix D

This Appendix shows reconstructions examples of the head and neck configuration of the image quality phantom.

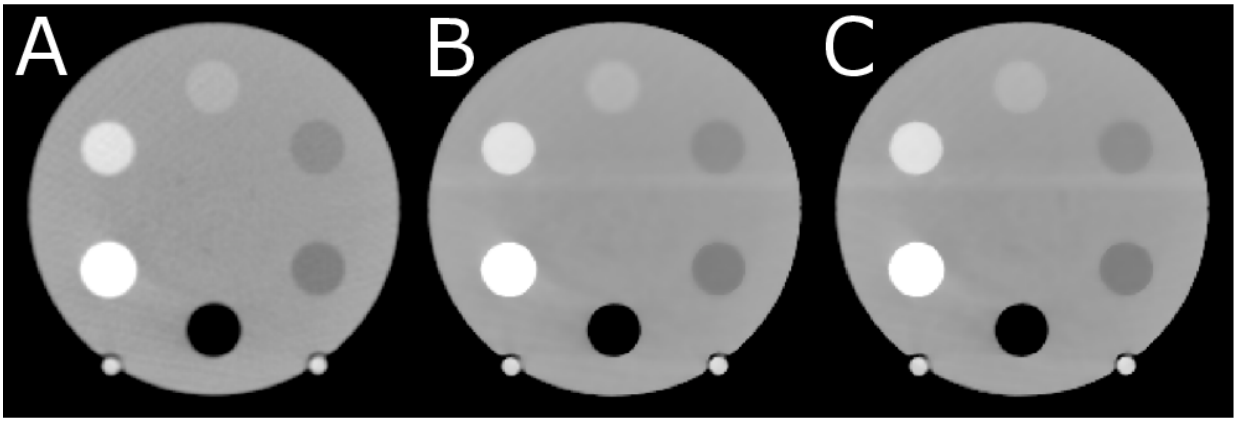

Figure D.1 Reconstruction examples of the head and neck configuration of the image quality phantom for (A) FDK (SE_{70}, h=1.0), (B) SE_{70} TV (N=10, θ = 5x10^{-4}), and (C) DE TNV ($DA_{88\%/12\%}$, LE component, N=10, θ = 10^{-3}. The window and level were kept constant for all images.

Appendix E

This Appendix displays the comprehensive results of the CNR and spatial frequency evaluation. The results for all three single energies, low and high energy dual-energy components, and all dose allocations are shown for the image quality and human male phantom.

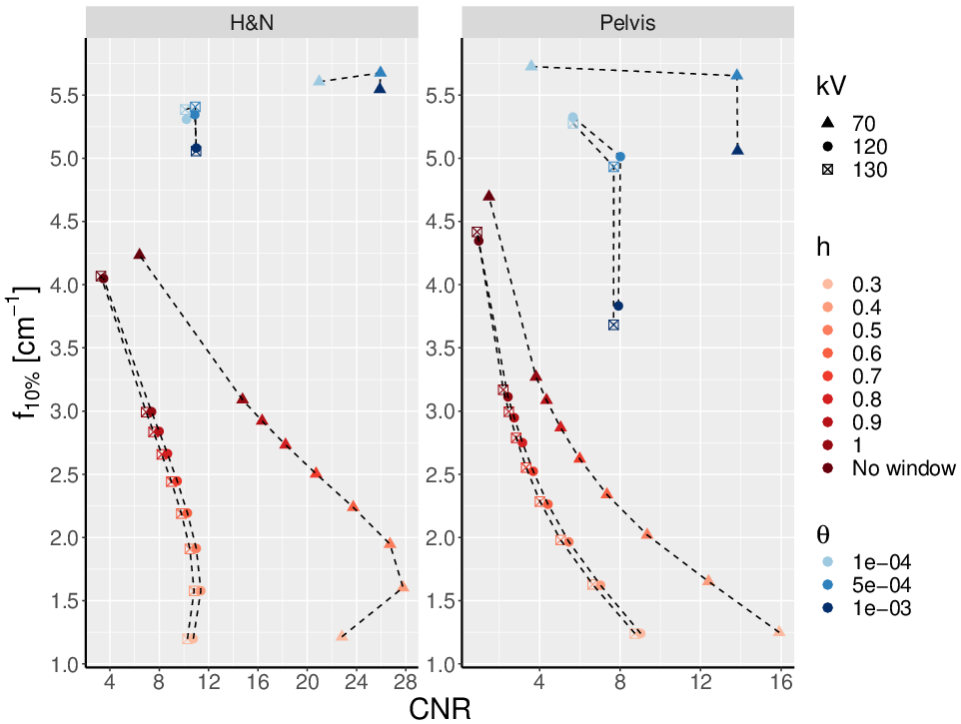

Figure E.1 CNR and spatial frequency of the different SE scans of both phantom configuration reconstructed with FDK and SE TV.

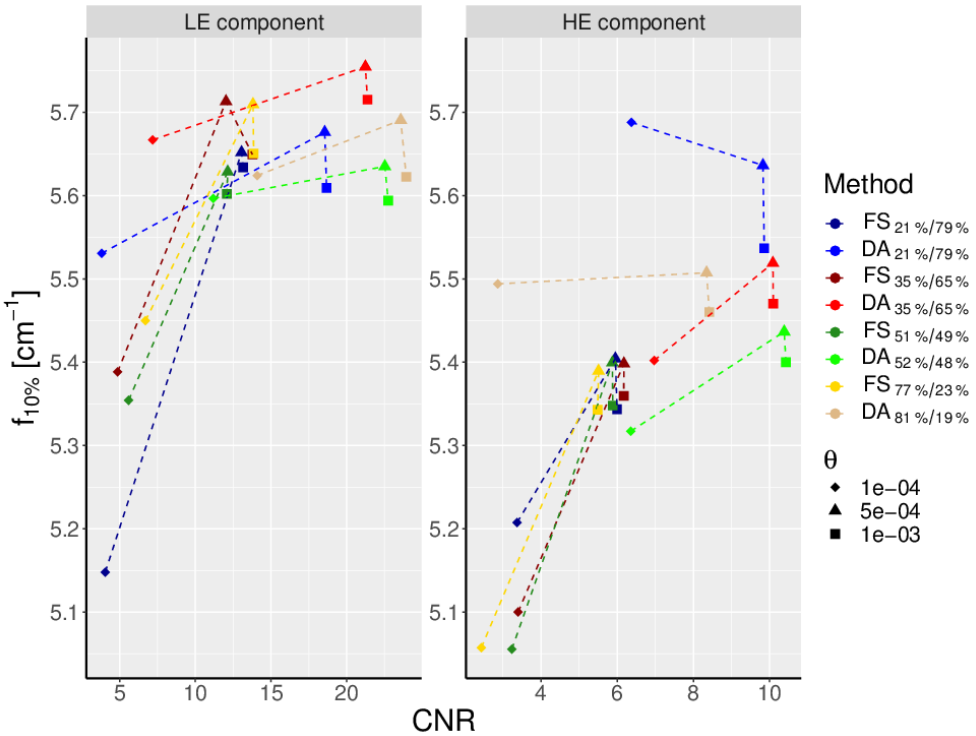

Figure E.2 CNR and spatial frequency of the DE scans of the H&N phantom configuration for different TNV weightings θ and LE%/HE% partitioning for both fast-switching (FS) and dual-arc (DA) acquisitions.

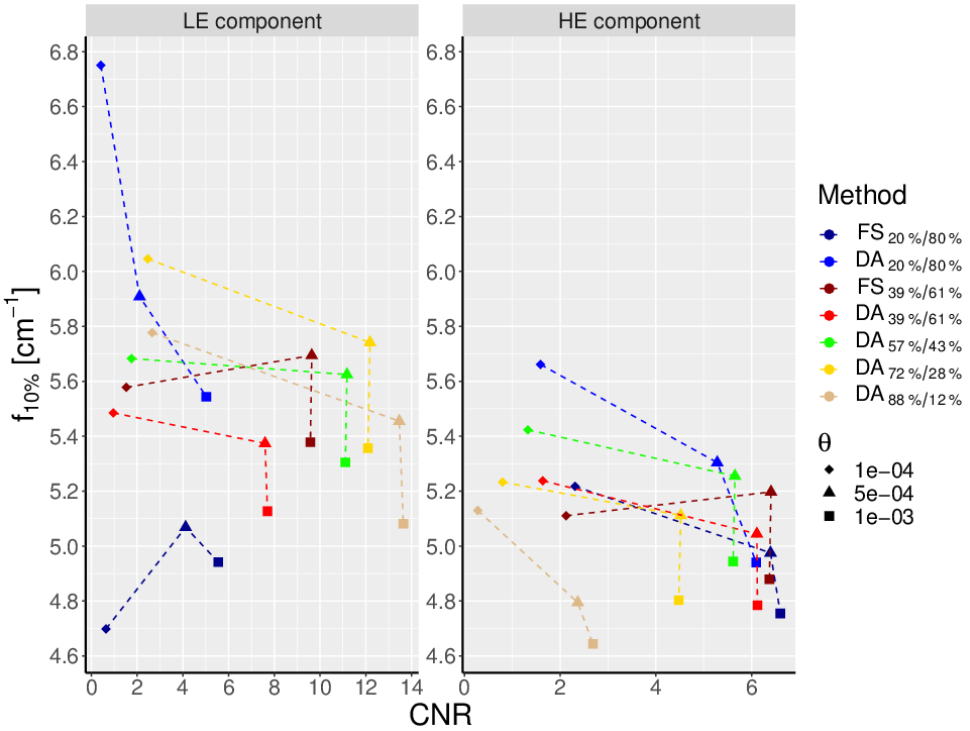

Figure E.3 CNR and spatial frequency of the DE scans of the pelvis phantom configuration for different TNV weightings θ and LE%/HE% partitioning for both fast-switching (FS) and dual-arc (DA) acquisitions.

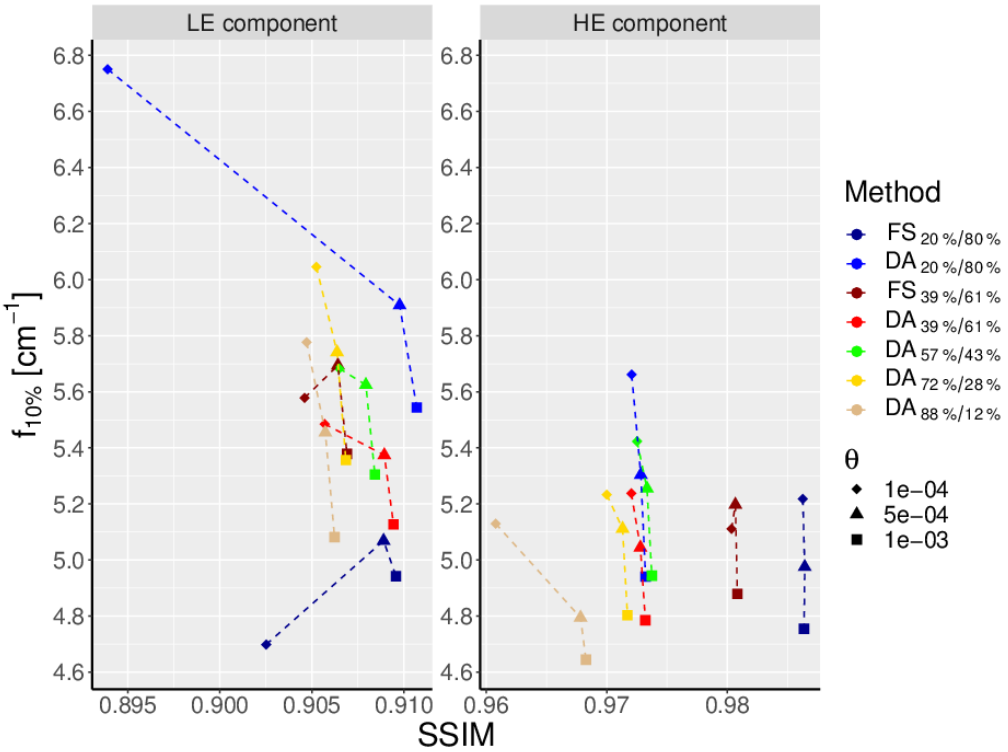

Figure E.4 SSIM and spatial frequency of the DE scans of the pelvis phantom configuration for different TNV weightings θ and LE%/HE% partitioning for both fast-switching (FS) and dual-arc (DA) acquisitions.

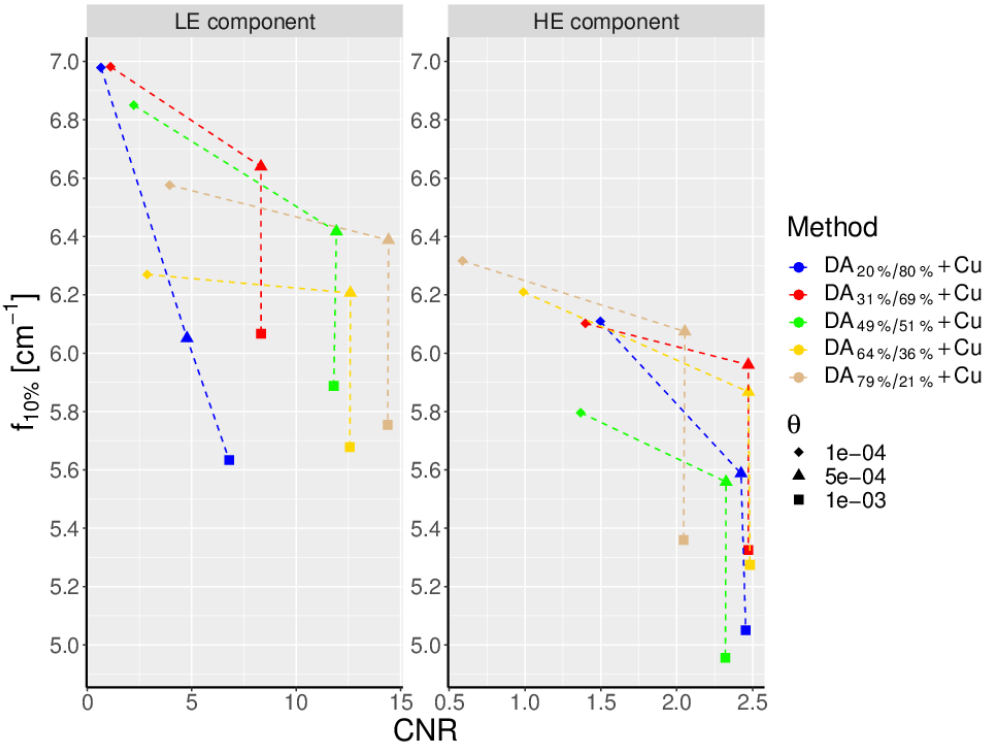

Figure E.5 CNR and spatial frequency of the DE scans of the pelvis phantom configuration with additional beam filtration for different TNV weightings θ and LE%/HE% partitioning.

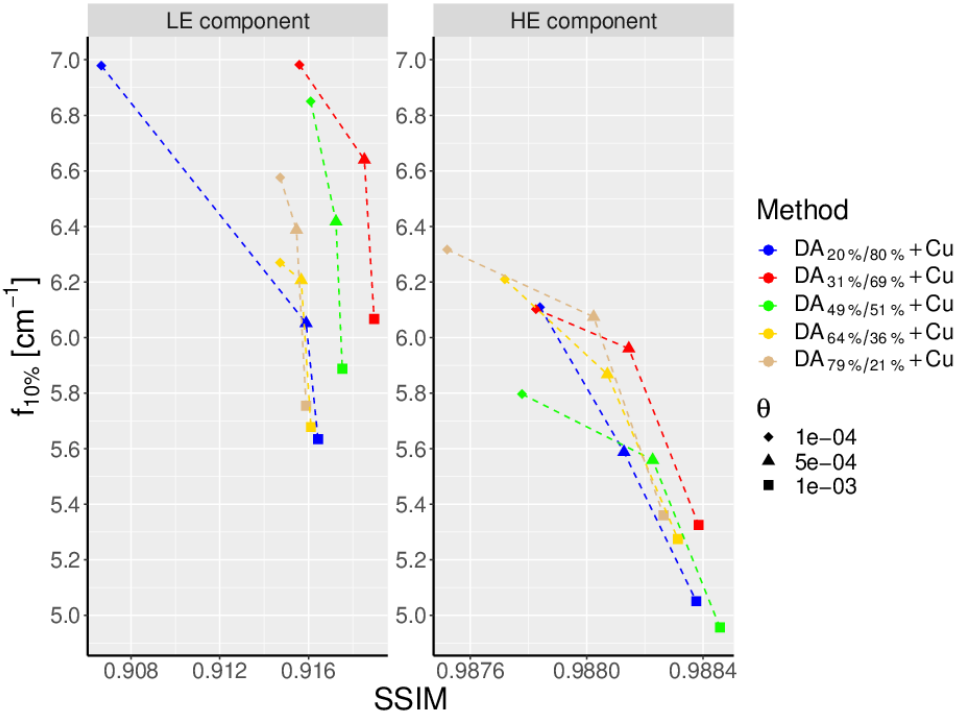

Figure E.6 SSIM and spatial frequency of the DE scans of the pelvis phantom configuration with additional beam filtration for different TNV weightings θ and LE%/HE% partitioning.

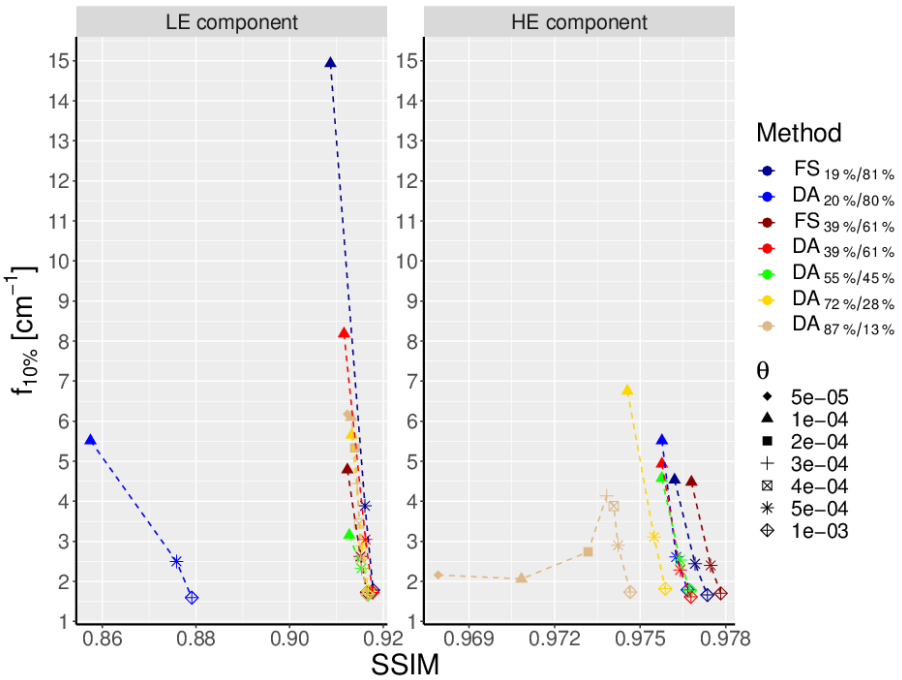

Figure E.7 SSIM and spatial frequency of the DE scans of the human male phantom for different TNV weightings θ and LE%/HE% partitioning.

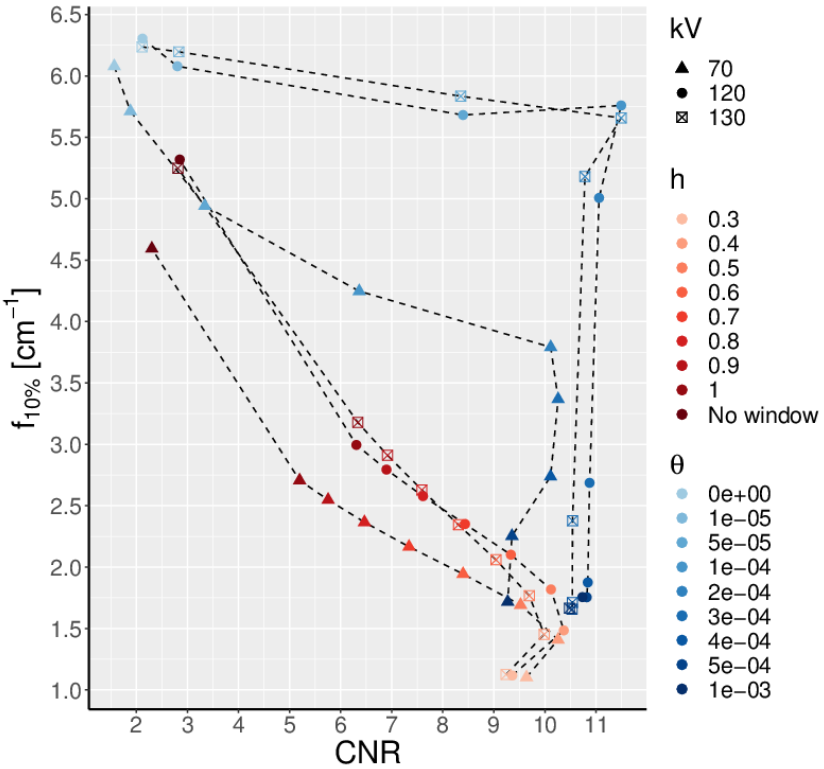

Figure E.8 CNR and spatial frequency of the different SE scans of the HMP reconstructed with FDK and SE TV.